Physical Origins of Thermal Properties of Cement Paste

Mohammad Javad Abdolhosseini Qomi,[*] Franz-Josef Ulm,[†] and Roland J.-M. Pellenq[‡]

Concrete Sustainability Hub, Department of Civil and Environmental Engineering, Massachusetts Institute of Technology, 77 Massachusetts Avenue, Cambridge, Massachusetts 02139, USA

(Received 18 October 2014; revised manuscript received 13 March 2015; published 17 June 2015)

Despite the ever-increasing interest in multiscale porous materials, the chemophysical origin of their thermal properties at the nanoscale and its connection to the macroscale properties still remain rather obscure. In this paper, we link the atomic- and macroscopic-level thermal properties by combining tools of statistical physics and mean-field homogenization theory. We begin with analyzing the vibrational density of states of several calcium-silicate materials in the cement paste. Unlike crystalline phases, we indicate that calcium silicate hydrates (CSH) exhibit extra vibrational states at low frequencies (< 2 THz) compared to the vibrational states predicted by the Debye model. This anomaly is commonly referred to as the boson peak in glass physics. In addition, the specific-heat capacity of CSH in both dry and saturated states scales linearly with the calcium-to-silicon ratio. We show that the nanoscale-confining environment of CSH decreases the apparent heat capacity of water by a factor of 4. Furthermore, full thermal conductivity tensors for all phases are calculated via the Green-Kubo formalism. We estimate the mean free path of phonons in calcium silicates to be on the order of interatomic bonds. This satisfies the scale separability condition and justifies the use of mean-field homogenization theories for upscaling purposes. Upscaling schemes yield a good estimate of the macroscopic specific-heat capacity and thermal conductivity of cement paste during the hydration process, independent of fitting parameters.

DOI: 10.1103/PhysRevApplied.3.064010

I. INTRODUCTION

With an average annual consumption rate of 1 m^3 per capita, concrete is the most-used man-made material on Earth. While well known for its appreciable load-bearing capacity, concrete's thermophysical properties are recognized to be important for both construction and use phases. During cement's exothermic hydration process, thermal stresses may cause early-age cracking, which may compromise the long-term serviceability of structures. The dimensional arguments indicate that these thermal stresses are inversely proportional to the thermal diffusivity of cement paste [1]. During the use phase, the thermophysical characteristics of concrete (and all other construction materials) affect the heating and cooling energy consumption of buildings via either heat conduction through the envelope or the thermal mass of the buildings, i.e., the tendency of a building to maintain a constant temperature despite outdoor temperature oscillations [2]. Both aggregates and the cement paste affect the thermal properties of concrete, however, the former is the dominant factor. Despite the importance of thermal properties of concrete, such studies are truly scarce and are limited to the macroscopic measurement of thermal properties of concrete [3–6] and cement paste [7–12]. More specifically, the interplay between chemistry and molecular properties of cement paste's constituents and their relation to macroscopic properties remain rather obscure.

This is in part associated with the hierarchical multiscale structure of cement paste. Here, by cement paste, we invoke a stoichiometric structural model of hardened cement paste rather than nonstochiometric materials found in hydrated cement systems. One can recognize at least four separate length scales in cement paste, when conceptualized in a four-level hierarchical thought model (see Fig. 1). At the nanoscale, molecular properties of individual phases become available via tools of statistical physics. In this investigation, we apply these methods to both crystalline and amorphous phases, namely, alite (Ca_3SiO_5 or C_3S), belite (Ca_2SiO_5 or C_2S), portlandite [$Ca(OH)_2$ or CH] and calcium silicate hydrates [$(CaO)_x(SiO_2)_1(H_2O)_y$ or CSH], where S, C, and H, respectively, stand for SiO_2, CaO, and H_2O in cement chemistry notation [see Figs. 1(a) and 1(c)].

[*]Also at Department of Civil and Environmental Engineering, Henry Samueli School of Engineering, E4130 Engineering Gateway, University of California, Irvine, Irvine, CA 92697-2175 USA.

[†]Also at the MultiScale Material Science for Energy and Environment, a joint MIT-CNRS laboratory at Massachusetts Institute of Technology, 77 Massachusetts Avenue, Cambridge, MA 02139, USA.

[‡]pellenq@mit.edu

Also at the MultiScale Material Science for Energy and Environment, a joint MIT-CNRS laboratory at Massachusetts Institute of Technology, 77 Massachusetts Avenue, Cambridge, MA 02139, USA, and Centre Interdisciplinaire des Nanosciences de Marseille, CNRS and Aix-Marseille Universite, Campus de Luminy, Marseille, 13288 Cedex 09, France.

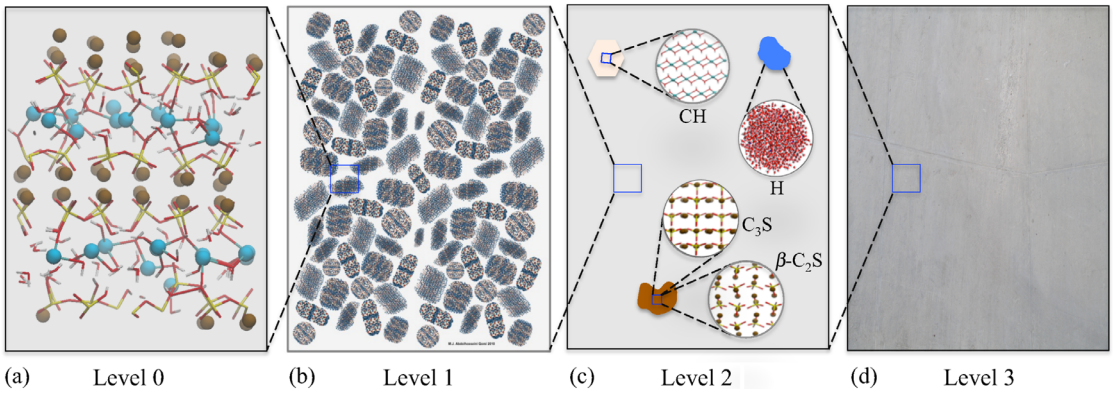

FIG. 1. A four-level thought model utilized for upscaling thermal properties of cement paste from the nanoscale to engineering scale. (a) Snapshot of a nanotexture of CSH at Ca:Si = 1.5. The brown and cyan spheres represent intra- and interlayer calcium ions. The Si—O bonds are shown by yellow-red bars. The water molecules and hydroxyl groups are depicted by red-white bars. The xy plane is parallel and the z axis is perpendicular to the calcium-silicate sheets. (b) The mesotexture of CSH constructed by agglomeration of randomly oriented CSH nanoparticles with size polydispersity. (c) The microtexture of hardened paste including anhydrous clinker phases (β-C_2S and C_3S), hydration products (CSH and CH), and pore space (saturated or dry). (d) The macrotexture of cement paste at the engineering scale.

The CSH gel at the mesoscale is considered to be comprised of polydisperse nanoscale CSH particles [13], based on the results of neutron scattering [14,15] and statistical nanoindentation experiments [16] [see Fig. 1(b)]. The physical properties of CSH gel at the mesoscale depend on the saturation level of the interparticle spacing and can be estimated via mean-field homogenization theories [17]. At the microscale, the CSH gel is regarded as an isotropic and homogeneous material with gel porosity that holds anhydrous cement clinkers and other hydration products together. This is consistent with a composite view of cement paste [see Fig. 1(c)]. In this sense, we regard laboratory measurements as the homogenized response of this multiscale porous composite [see Fig. 1(d)].

We have previously studied mechanical properties [18–23] and diffusion dynamics [24] of cement paste at the molecular level. In this paper, we focus on understanding the physical origins of macroscopic thermal properties of cement paste, starting from the atomic scale. The paper is organized in seven sections. Section II describes the molecular structures of calcium-silicate phases in cement paste and provides details of atomistic simulations. We dedicate Sec. III to a thorough analysis of vibrational densities of states (VDOS) of all phases, because they are at the origins of equilibrium and nonequilibrium thermal properties of materials. Subsequently, we employ VDOSs in conjunction with MD calculation in Sec. IV to measure specific-heat capacity values at constant volume and pressure. Section V highlights the nonequilibrium thermal properties of all phases at the nanoscale from equilibrium molecular dynamics using the Green-Kubo approach. In Sec. V, we also provide a full measurement of the thermal conductivity tensor, which is accompanied by a discussion of the mean free paths of phonons and their effect on the heat transport in complex crystalline and amorphous materials. Subsequently, we use mean-field homogenization techniques in Sec. VI to provide a seamless link between the nano- and macroscopic thermal properties, and we compare our predictions with experiments. Section VII draws final conclusions and summarizes our findings.

II. METHODS

A. Molecular models

The molecular structure of solid phases in hardened cement paste vary from crystalline to amorphous, depending on the phase and its chemical composition. The anhydrated clinker phases (alite and belite) and portlandite are crystalline. From a crystallography viewpoint, alite is a chemically modified form of pure tricalcium silicate (C_3S), exhibiting a series of reversible phase transitions upon heating and cooling [25]. The atomic structure of alite polymorphs is similar, differing in the orientation of isolated silica tetrahedra (SiO_4^{4-}), coordination of calcium (Ca^{2+}) and oxygen (O^{2-}) atoms in ionic sites, and hence symmetry groups [26]. In the present work, we choose the M3 polymorph of C_3S, the most abundant polymorph in cement clinkers, refined from single crystal by de la Torre *et al.* [27]. Belite is similar to alite in many aspects. It is a chemically modified form of delicacies silicate (C_2S), which also exhibits a sequence of reversible phase transitions with temperature [25]. The atomic structure of belite is consisted of isolated SiO_4^{4-} groups surrounded merely by Ca^{2+} cations. Belite has several polymorphs such as α'_H, α'_L, and β, which are derived from the α form by decreasing symmetry because of disorder in silica groups and subsequent modifications in calcium atoms [28]. In the present study, we employ the β-C_2S polymorph after Midgley [29], as it is the most dominant polymorph in ordinary Portland

cement (OPC) systems [30]. The M3 C_3S and β-C_2S phases are rarely found in pure forms and usually contain minor Al^{3+}, Mg^{2+}, and Fe^{3+} substitutions that modulate their stability, solubility, and chemical reactivity [31]. These substitutions are neglected in the present study because they are attributed to a relatively small mass fraction of the OPC clinker. Beside clinker phases, portlandite (CH), one of the major hydration products in OPC systems, is also crystalline and is a fairly well-known mineral. It consists of planar Ca—O bonds with dangling hydroxyl groups pointing to the interlayer spacing. In this work, we adopt a crystalline structure of portlandite after Henderson *et al.* [32], which identifies the position of protons via ^{1}H NMR.

The nanotexture of CSH strongly depends on its chemical composition. In addition to 11-Å tobermorite, we utilize a set of 150 molecular models constructed to cover a wide range of calcium-to-silicon ratios (Ca:Si), spanning from 1.1 to 2.1 [18,24]. Following a combinatorial scheme, these models are constructed by structural and chemical modification of 11-Å tobermorite [33,34]. The Ca:Si ratio of 11-Å tobermorite is systematically increased by randomly removing charge-neutralized SiO_2 groups from its infinitely long silica chains. We create five models for each Ca:Si ratio to ensure proper statistical sampling by altering the arrangement of vacancies. As shown in Fig. 1(a), CSH consists of negatively charged defective calcium-silicate layers separated by an interlayer spacing, which is filled with water molecules and charge-balancing calcium cations. Vacancies in the silicate chains provide possible adsorption sites for water molecules. The adsorption of water molecules in defect sites is performed via grand canonical Monte Carlo (GCMC) simulation ensuring equilibrium with bulk water at constant volume and room temperature. Some of the above-mentioned adsorbed water molecules are chemically unstable and dissociate into hydroxyl groups and protons upon first-principle or reactive force-field modeling. REAXFF potential is subsequently utilized to enforce reaction between the interlayer water molecules and defective calcium-silicate layers [18,35]. These molecular structures are extensively validated against nuclear magnetic resonance, elastic and inelastic neutron scattering, x-ray diffraction, and drying experiments (for further details on model constructions and validations, see Abdolhosseini *et al.* [18,24]). These realistic molecular structures are consistent with the averaged stoichiometry of $Ca_xSiO_{2.75}(OH)^{Ca}_{0.85(x-1)}(OH)^{Si}_{1.15(x-1)+0.5} \times[0.8(x-1)+0.3]H_2O$, where x is the Ca:Si ratio and $(OH)^{Ca}$ and $(OH)^{Si}$ represent hydroxyl groups coordinated to interlayer calcium atoms and silica groups, respectively. The collective topological observation of these 150 models indicates that, while at low Ca:Si ratios (Ca:Si < 1.2) CSH exhibits a lamellar crystalline structure with strong transversely isotropic mechanical response; the structure of CSH at high Ca:Si ratios (Ca:Si > 1.7) is fairly amorphous, exhibiting isotropic mechanical properties [18].

B. Atomistic simulation and force fields

In this work, we use molecular dynamics (MD), energy minimization, and phonon analysis techniques to study thermal properties of clinker phases and hydration products using LAMMPS [36], GULP [37,38], and a series of inhouse codes. In MD, the equations of motion are integrated via the velocity-Verlet algorithm with periodic boundary conditions applied in all directions. After performing extensive convergence studies, the suitable time steps are found to be as small as 0.1 fs for CSH and portlandite and 1 fs for clinker phases. For crystalline phases, we create a relatively large supercell containing roughly 1000 atoms. The sizes of CSH simulation boxes are 5 to 6 times larger than the characteristic medium-range length scale of calcium-oxide layers and silica chains [18]. Therefore, we expect no size effect in our simulations. Initially, all CSH models and the crystalline phases are relaxed in isobaric isothermal ensemble (NPT) at room temperature and pressure of 0 atm. To exclude the impact of fictitious forces on the trajectories of atoms from affecting velocities and heat fluxes along the MD trajectory, further simulations are carried out in the microcanonical ensemble (NVE). In order to properly calculate the statistical errors for each model, 10 independent simulations are performed, each 10^6 time steps long. Core-only CSH force-field (FF) [39] potential is used in simulations (see the Supplemental Material [40], Sec. A and Tables I–IV, for force-field details). To avoid the computational expenses incurred by the calculation of Coulombic interactions in real and reciprocal spaces, such interactions are calculated via the Wolf method [41]. We further investigate the transferability of CSH FF potential to crystalline phases by comparing its predictions of lattice structure and mechanical properties including bulk k, shear g moduli, and with Poisson's ratio ν, against existing experimental data [42–46] (see the Supplemental Material [40], Sec. B and Tables V and VI, for potential validations).

III. VIBRATIONAL DENSITIES OF STATES

In dielectric solids, the atomic vibrations are at the origin of nanoscale thermal properties. At low temperatures, such vibrations are considered to be harmonic, which become progressively anharmonic with increasing temperature. These collective harmonic vibrations, the so-called phonons, are closely related to thermodynamic properties such as free energy, heat capacity, and thermal conductivity. The vibrational density of state, also known as the phonon density of state, over frequency $g(\omega)$ characterizes the number of phonons having a frequency in the range of ω and $\omega + d\omega$,

$$g(\omega) = \frac{1}{3N-3}\sum_{s=4}^{3N}\delta(\omega-\omega_s), \tag{1}$$

where N is the number of atoms and ω_s is the sth eigen vibrational frequency. The first three frequencies are neglected as they are associated with translational motion

of the solid. Within the harmonic approximation theory (i.e., small atomic displacements from equilibrium positions), $g(\omega)$ can be computed via two different approaches. The first method is the eigenvalue decomposition of the dynamical matrix (EDDM), which is based on the notion of the normal mode analysis [47]. Any atomic vibration can be considered as a linear superposition of normal modes, i.e., the eigenvectors of the dynamical matrix $\{e^n, n = 1, \ldots, N\}$,

$$\sum_{q,\beta} D_{p,\alpha;q,\beta} e^n_{j\beta} = \omega_n^2 e^n_{p\alpha}, \tag{2}$$

where p and q denote the atoms, α and β are the Cartesian coordinate indices, and $\mathbf{D}$ is the dynamical matrix defined as

$$D_{pq,\alpha\beta}(k) = \frac{1}{\sqrt{m_p m_q}} \left(\frac{\partial^2 U_{\text{lat}}}{\partial\alpha\partial\beta} \right) e^{ikr}, \tag{3}$$

with m_p the mass of the pth atom, U_{lat} is the lattice energy, and e^{ikr} is the phase factor. There are a number of possible choices for the set of k points in the first Brillouin zone, the primitive cell in the reciprocal space. The supercell of crystalline models and CSH contain, respectively, roughly 1000 and 500 atoms. Although these supercells are relatively large, a fine $15 \times 15 \times 15$ grid of k points with the Monkhorst-Pack scheme [48] is utilized to ensure proper sampling of the Brillouin zone.

The second method to compute $g(\omega)$ employs the Fourier transform of the velocity autocorrelation function (VACF) over a long-enough molecular-dynamics trajectory,

$$g(\omega) = \frac{1}{Nk_BT} \sum_{j=1}^{N} m_j \int_{-\infty}^{\infty} \langle \mathbf{v}_j(t) \cdot \mathbf{v}_j(0) \rangle e^{i\omega t} dt, \tag{4}$$

where ω is the frequency, k_B is the Boltzmann constant, T is the temperature, $\mathbf{v}_j(t)$ is the velocity, and the dot denotes the dot product. Due to the oscillatory nature of VACF ($\langle \mathbf{v}_j(t) \cdot \mathbf{v}_j(0) \rangle / \langle \mathbf{v}_j(0) \cdot \mathbf{v}_j(0) \rangle$), femtosecond and even subfemtosecond resolution is required to fully capture $g(\omega)$ (see VACF insets in Fig. 2).

Figures 2(a), 2(c), 2(e), and 2(g) present the VDOS of, respectively, β-C_2S, C_3S, CH, and a CSH model with Ca:Si = 1.5, showing that VACF and EDDM yield almost identical results for all molecular models. To better classify the different atomic bond contribution to the VDOS in complex materials such as CSH, we divide the phonon spectrum into five distinct vibrational bands, denoted I through V in Fig. 2(g). We recognize the underlying atomic and molecular vibrations populating the aforementioned bands by decomposing the VACF into its partial contributions, VACF_γ, where $\gamma = \{\text{Si}, \text{Ca}, \text{O}, \text{OH}, \text{H}_2\text{O}\}$. These partial contributions to VDOS are presented in Figs. 2(b), 2(d), 2(f), and 2(h) for β-C_2S, C_3S, CH, and CSH,

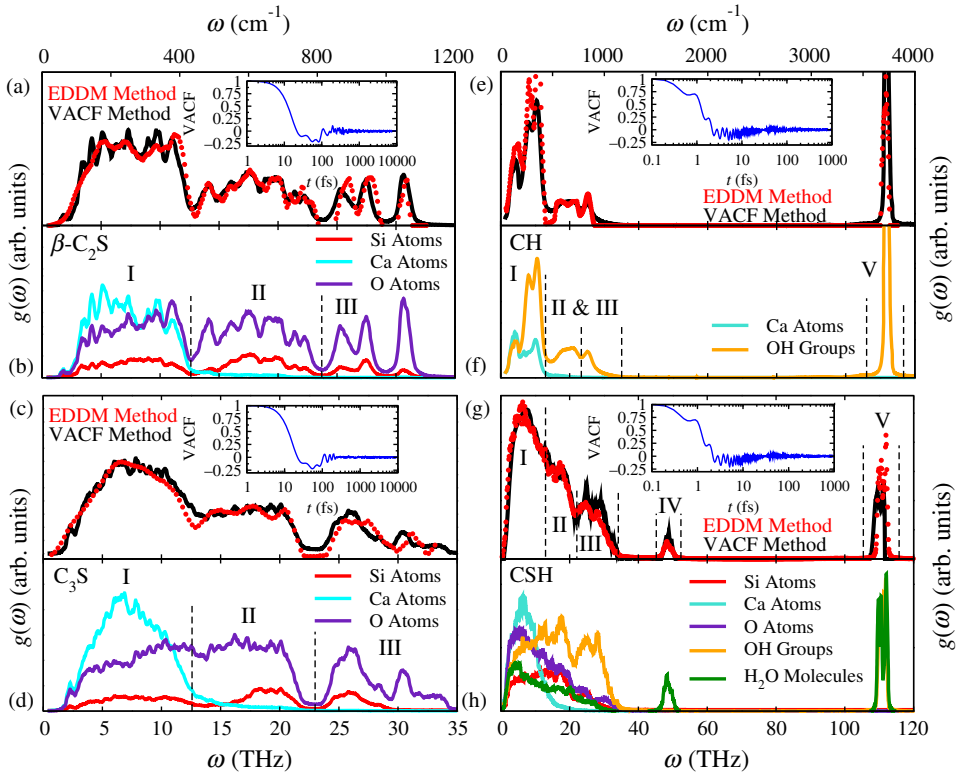

FIG. 2. Vibrational density of state (VDOS) for β-C_2S, C_3S, CH, and a CSH sample with Ca:Si = 1.5. VDOS calculated via the eigenvalue decomposition of the dynamical matrix (EDDM) and Fourier transformation of the velocity autocorrelation function (VACF) for (a) β-C_2S, (c) C_3S, (e) CH, and (g) CSH. The insets shows the evolution of VACF spanning 4 orders of magnitude. Decomposition of the VDOS to contributions from different atomic and molecular species for (b) β-C_2S, (d) C_3S, (f) CH, and (g) CSH.

respectively. The VDOS partial contributions unanimously assert that the peak in the I band is clearly attributable to the vibration of Ca—O bonds. This is in full agreement with the near-infrared spectroscopy experiments of Yu *et al.* [49], associating $\omega < 400$ cm^{-1} to stretching of Ca—O bonds. Unlike Ca—O phonons, vibrations of SiO_4 units extend over a large band from 0 to 35 THz. As studied in detail for amorphous silica [50], the Si—O frequencies in the I band are related to the acousticlike rigid-body rotation of SiO_4 tetrahedra units in the silica network. In the case of β-C_2S and C_3S, the vibrations in this band are associated with the isolated rigid-body rotation of silica monomers. In the case of CSH, however, these vibrations are related to the coupled rotation of SiO_4 units in the silica chains. The simulation results indicate that the II band, 400 cm^{-1} $< \omega <$ 750 cm^{-1}, is dominated by the vibration of silica tetrahedra units. This is in agreement with a midinfrared experiment [49] relating this band to stretching of Si—O bonds, and symmetric and asymmetric bending of Si—O—Si angles. For silica glass, Taraskin and Elliot [50] suggested that the vibrations in this frequency window are associated with a complex hybridization of acoustic and optical modes manifested in quasilocalized internal stretching and bending of SiO_4 units. Furthermore, the III band in the range of 750 cm^{-1} $< \omega <$ 1200 cm^{-1} is also populated with silica tetrahedra vibrations. In β-C_2S and C_3S, these vibrations are accumulated into peaks that are associated with highly localized longitudinal and transverse optical modes that correspond to stretching and bending of silica monomers. In particular for CSH, the III band is mainly associated with the vibration of Q_1 and Q_0 sites containing silanol groups (Si—OH), due to the strong presence of an OH signal in the partial VDOS. The vibrational frequencies in region IV result from the inplane bending of the H—O—H angle of water molecules because this vibrational frequency is only present in the partial VDOS of water molecules and it is absent in VDOS of portlandite. The V band represents both the symmetric and asymmetric stretching of O—H bonds in water molecules, the stretching of hydroxyl groups coordinated to both Ca and Si atoms in CSH, and the stretching of hydroxyl groups in portlandite.

One of the most striking features in VDOS of glasses, and glass-forming and supercooled liquids is the presence of a universal excess of states (EOS) compared to that predicted by the Debye model ($g_D \propto \omega^2$) in the low-frequency region [51]. This EOS is responsible for the anomalies of the heat capacity and thermal conductivity of glasses at low temperatures [52]. Highlighted by a broad peak in the THz region (< 5 THz) when plotting $g(\omega)/\omega^2$, this peak is referred to as the boson peak (BP). The BP can be experimentally identified via Raman spectroscopy and one-phonon scattering cross section in inelastic neutron scattering [53]. Despite decades of work, the origin of BP remains an open question in condensed matter physics and

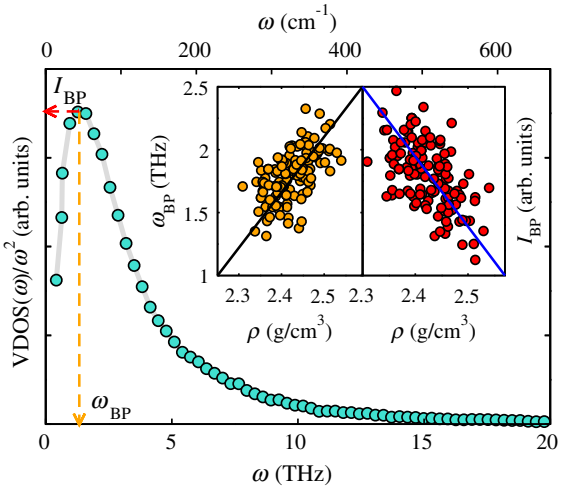

FIG. 3. Boson peak identification in a CSH sample with Ca:Si = 1.5. The inset shows the location (ω_{BP}) and intensity (I_{BP}) of the boson peaks for all 150 CSH models in terms of their density calculated via atomistic simulation.

material science [54]. Existing theoretical models explain BP via different mechanisms such as phonon-saddle transition in the energy landscape [55], local vibrational modes of clusters [56], locally favored structures [57], liberation of molecular fragments [58,59], vibrations in anharmonic potentials [60], and anomaly in transverse phonon propagation related to the Ioffe-Regel limit [54]. Exhibiting common features of disordered and amorphous materials [18,19], the VDOS of CSH presents a BP in the THz region as shown in Fig. 3. The BP is characterized by the peak position ω_{BP} and the peak intensity I_{BP}. As observed in many glass-forming materials such as polybutadiene, polystyrene [53], LiCl [61], and B_2O_3 [62], ω_{BP} is usually found to be shifted to lower frequencies with increasing temperature. As an exception to this rule [63], ω_{BP} in silica is slightly shifted to the left with decreasing density [64,65]. The analysis of all CSH models indicates that the composition affects both positions and intensities of BPs. When expressed in terms of density in the inset of Fig. 3, ω_{BP} of CSH decreases with increasing density and its I_{BP} behaves conversely. The correlation between the CSH density and its BP properties are analogous to the pressure dependence of the BP observed in silica [64], $Na_2FeSi_3O_8$ [66], and polymers [67].

IV. NANOSCALE HEAT-CAPACITY CALCULATIONS

Heat capacity is a thermal property of materials at equilibrium that links variations of internal energy (U) and temperature. The internal energy of an insulating solid is the sum of lattice (U_{lat}), vibrational (U_{vib}), rotational (U_{rot}), and translational (U_{tra}) energetic contributions. At low temperatures, considerably below the Debye temperature [68], the rotational and translational contributions

(U_{rot} and U_{tra}) are negligible compared to the other two components; hence, $U \simeq U_{lat} + U_{vib}$. U_{vib} can be described as the number of phonons occupying a particular state $n(\omega)$ times their vibrational energy level $h\omega$, that is,

$$U_{vib} = \int_0^\infty h\omega\left(n(\omega) + \frac{1}{2}\right)d\omega, \quad (5)$$

where h is the Plank constant and $h\omega/2$ is the zero-point energy contribution. Following Bose-Einstein statistics, $f_{BE}(\omega) = (e^{-h\omega/k_BT} - 1)^{-1}$ is the probability distribution of a boson particle occupying a specific quantum state in the thermal equilibrium. Thus, the occupation level is the degeneracy of the vibrational state, described through $g(\omega)$, times the probability of the presence of phonons at that specific state; i.e., $n(\omega) = g(\omega)f_{BE}(\omega)$. This yields the kinetic energy in terms of vibrational density of states in Eqs. (1) and (4). The specific-heat capacity at constant volume can then be calculated from $c_v = (\partial U/\partial T)_v = (\partial U_{vib}/\partial T)_v$, noting that U_{lat} does not depend on T at constant volume. Experimental measurement of c_v is rather difficult because it requires maintaining constant volume throughout the experiment. Therefore, laboratory measurement of specific-heat capacity at constant pressure c_p is more popular. From thermodynamics, c_v and c_p are related via

$$c_p - c_v = T\frac{\alpha^2}{\rho\beta}, \quad (6)$$

where ρ is the density calculated in atomistic simulation, $\alpha = (1/V)(\partial V/\partial T)_P$ is the coefficient of thermal expansion, and $\beta = -(1/V)(\partial V/\partial P)_T$ is the compressibility which is the reciprocal of bulk modulus. Here, we calculate these two coefficients via a finite difference approach in an isobaric-isothermal (NPT) ensemble. To this end, three 10-ns-long simulations are performed on a number of CSH samples, β-C_2S, C_3S, and CH at (300 K, 0 atm), (310 K, 0 atm), and (300 K, 100 atm). The results for β-C_2S, C_3S, CH, 11-Å tobermorite, and a CSH model with stoichiometry of $C_{1.75}SH_{2.0}$ are summarized in Table I. The compressibility of the crystalline phases presented in the Supplemental Material [40], Table II, are almost identical with those calculated at zero temperature. The densities of the crystalline phases are compared to experimental values of bulk measurements [69] and crystallographic density [27,29,32]. Since the effect of porosity and impurities are neglected in our atomistic simulations, our predicted densities are closer to crystallographic measurements than bulk measurements. The CSH compressibility increases with increasing Ca:Si ratio, 1.5×10^{-11} Pa$^{-1} < \beta_{CSH} < 1.8 \times 10^{-11}$ Pa^{-1}. These results are in full agreement with zero-temperature calculations of CSH's bulk modulus [18] k_{CSH}, indicating a decrease in k_{CSH} with increasing Ca:Si ratio, 55 GPa $< k_{CSH} <$ 65 GPa. CSH's coefficient of thermal expansion calculated from MD is $4.5(\pm 0.9) \times 10^{-5}$ K^{-1}, in agreement with 4.2×10^{-5} K^{-1} microthermoporomechanics backanalysis [70]. The CSH density is found to decrease with increasing Ca:Si ratio, 2.55 g/cm^3 $> \rho_{CSH} >$ 2.35 g/cm^3. At a low Ca:Si ratio, the density is close to that of experimental density reported for tobermorite minerals [71,72]. The density of CSH at a high Ca:Si ratio is slightly lower than values obtained from neutron scattering experiments [14,73] and is close to recent experimental values reported by Muller *et al.* [74], after subtracting the monolayer of water adsorbed on the external surface of CSH nanoparticles. Having computed α, β, and ρ, the difference between c_p and c_v is calculated to be in the range of 0.002–0.025 J/g K for different calcium-silicate systems.

Table I presents the specific-heat capacities at constant volume and pressure for β-C_2S, C_3S, and CH. The atomistic simulation predictions of constant-pressure heat capacities are in very good agreement with low-temperature heat-capacity measurements [75] and with values calculated from fitted c_p-T relations [69]. We regard this agreement as further validation of the transferability of CSH FF potential to other calcium-silicate systems that allows refining not only structural but also vibrational properties. Figure 4 displays the specific-heat capacity of both dry (all molecular interlayer water removed) $c_{v,p}^{dry}$ and hydrated $c_{v,p}^{hyd}$ CSH in terms of the Ca:Si ratio. The specific-heat capacities in both dry and hydrated samples increase almost linearly with Ca:Si with a minor scatter attributable to the polymorphic structure of CSH [18]. Similar to the experimentally observed increase in heat capacity of rocks [76] and Vycor glass [77], the heat

TABLE I. Equilibrium properties of β-C_2S (belite), C_3S (alite), CH (portlandite), $C_{1.0}SH_{0.5}$ (11-Å tobermorite), and $C_{1.75}SH_{2.0}$ including density, compressibility, coefficient of thermal expansion, constant-volume, and constant-pressure specific-heat capacities calculated using CSH FF potential and compared against available experimental measurements.

	c_v (J/g K)	ρ (g/cm^3)		β (1/Pa)	α (1/K)	c_p (J/g K)	
	Sim.	Sim.	Expt.	Sim.	Sim.	Sim.	Expt.
β-C_2S	0.69	3.55	3.31 [69], 3.36 [29]	8.18×10^{-12}	4.99×10^{-5}	0.72	0.71 [69], 0.75 [75]
C_3S	0.68	3.57	3.13 [69], 3.55 [27]	9.53×10^{-12}	4.95×10^{-5}	0.71	0.72 [69], 0.75 [75]
CH	1.14	2.25	2.25 [69], 2.08 [32]	3.47×10^{-11}	9.91×10^{-5}	1.14	1.15 [69]
$C_{1.0}SH_{0.5}$	0.87	2.55	2.48 [71], 2.46 [72]	1.47×10^{-11}	4.50×10^{-5}	0.89	
$C_{1.75}SH_{2.0}$	0.95	2.40	2.47 [74], 2.60 [14]	1.82×10^{-11}	4.50×10^{-5}	0.97	

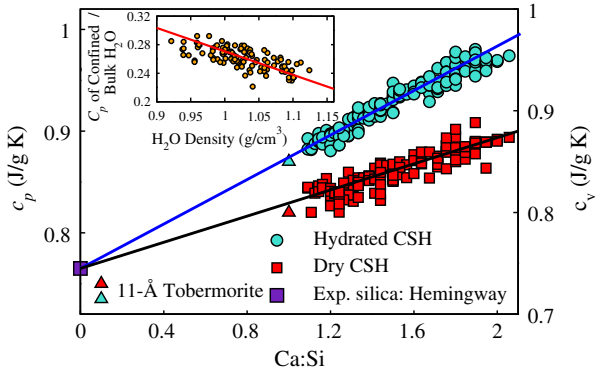

FIG. 4. The effect of Ca:Si ratio on specific-heat-capacity values at constant volume and pressure for dry and hydrated CSH models and 11-Å tobermorite. The black and blue lines are fitted to the atomistic simulation data. These lines intersect at a point corresponding to the heat capacity of amorphous silica [78]. The inset indicates the relation between the Voronoi density of the nanoconfined water and its apparent heat capacity measured as the difference between the heat capacity of dry and hydrated CSH.

capacity of hydrated CSH is higher than that of dry samples. The constant-pressure specific-heat capacities can be written in the form of $c_p^{\mathrm{dry}} = 0.66x + 0.75$ and $c_p^{\mathrm{hyd}} = 1.00x + 0.75$, where x is the Ca:Si ratio. The two lines intersect at 0.75 J/g K at Ca:Si = 0, which is the experimental heat capacity of amorphous silica (devoid of calcium) at room temperature [78]. The specific-heat capacity of CSH is less than those observed for cement pastes with different water-to-cement ratios and saturation degree [7]. The heat capacity of cement paste is a composite response of different phases, including anhydrous clinker, portlandite, and water, that is discussed in Sec. VI.

The difference between dry and hydrated samples indicates the effect of interlayer water on the heat capacity of CSH. In fact, the apparent heat capacity of nanoconfined water can be considered as the difference between the specific-heat capacities of wet and dry CSH, $\Delta c_p = c_p^{\mathrm{hyd}} - c_p^{\mathrm{dry}} = 0.34x$. According to the average chemical composition (see Sec. II A), the interlayer water content scales with $\Delta M_w = 0.8x$. Since $\Delta c_p/\Delta M_w < 1$, the heat capacity of the nanoconfined water decreases with an increasing Ca:Si ratio. It is instructive to display the variation of the heat capacity of nanoconfined water in terms of its Voronoi density rather than the Ca:Si ratio. To this end, the Voronoi density of interlayer water is measured via a Voronoi tessellation algorithm, which finds a portion of space that is closer to a given water molecule than any other atom in the molecular structure [24,79]. The inset of Fig. 4 shows the relation between the normalized apparent heat capacity and the Voronoi density of the nanoconfined water. The heat capacity of water in the ultraconfining interlayer spacing of CSH ($d < 1.0$ nm) is noticeably smaller than that of bulk water at room temperature, roughly 4.2 J/g K [80]. This is in full agreement with Bentz's postulate stating that the heat capacity of chemically and physically bound water within the hydration gel should be significantly lower than that of bulk water [7]. Similar to dynamical properties [24], the heat capacity of nanoconfined water in CSH and its trend with density behaves like supercooled water. In fact, although being at room temperature, Δc_p is on the order of those observed at 150 K [81]. This is mainly due to the strong interactions between the water molecules and the substrate [24].

V. NANOSCALE HEAT-CONDUCTIVITY CALCULATIONS

The thermal conductivity $\mathbf{K}$ of a dielectric material is a second-order tensor relating the temperature gradient $\nabla\mathrm{T}$ to the heat flux $\mathbf{q}$ through Fourier's law, $\mathbf{q} = \mathbf{K} \cdot \nabla\mathrm{T}$. There are three methods to calculate $\mathbf{K}$ for an insulating solid via MD simulation: the equilibrium Green-Kubo method (GK); direct application of Fourier's law within a steady-state conduction regime in a nonequilibrium framework (known as the direct method); and a transient nonequilibrium method. In this work, the GK approach is employed because it is less size dependent, does not involve imposing unrealistic temperature gradients in the simulation cell, and it yields the full thermal-conductivity tensor. Heat flux in a multiparticle system can be simply written as [82]

$$\mathbf{q} = \frac{1}{V}\frac{d}{dt}\sum_{i=1}^{N}\mathbf{r}_i H_i, \tag{7}$$

where $\mathbf{r}_i$ and H_i stand for, respectively, the position vector and the total Hamiltonian (kinetic plus potential energies) of the ith particle in the system, whereas V is the volume. To exclude the numerical errors arising from the calculation of a time derivative in the finite-difference approach, the above expression can be rearranged considering the mathematical form of the interatomic potential. Assuming that the angular contributions in the CSH FF potential are equally distributed among all atoms in a water molecule, H_i can be expressed in terms of its components via [83]

$$H_i = \frac{1}{2}m_i\mathbf{v}_i \cdot \mathbf{v}_i + \frac{1}{2}\sum_j u_2(r_{ij}) + \frac{1}{6}\sum_{kj} u_3(\theta_{jik}), \tag{8}$$

where $\mathbf{v}_i$ is the velocity of ith particle, u_2 represents pairwise energy terms between the ith particle and its jth neighbor located r_{ij} apart from each other, and includes van der Waals, Coulomb interactions via Wolf summation method, and bond-stretching terms. The u_3 energy term considers the bending energy of the central θ_{ijk} angle in water molecules. By substituting Eq. (8) in Eq. (7), an alternative expression for heat flux is achieved,

$$\mathbf{q} = \frac{1}{V}\sum_{i=1}^{N}[e_i\mathbf{v}_i - V\mathbf{S}_i \cdot \mathbf{v}_i], \tag{9}$$

where e_i is the kinetic energy and $\mathbf{S}_i$ is the atomic virial stress tensor, which can be expressed in terms of two- and three-body potential terms as [84]

$$\mathbf{S}_i = \frac{1}{2V}\sum_{j=1}^{N_p,N_b} \mathbf{r}_{ij} \otimes \mathbf{F}_{ij} + \frac{1}{6V}\sum_{i=1}^{N_a} (\mathbf{r}_{ij} + \mathbf{r}_{ik}) \otimes \mathbf{F}_{ijk}, \quad (10)$$

where $\otimes$ is the dyadic product in tensor notation, $\mathbf{F}_{ij}$ the force due to pair potentials, and $\mathbf{F}_{ijk} = -\boldsymbol{\nabla}_i u_3(\theta_{jik})$ is a three-body force term. We implement the above heat-flux formulation in GULP source code [37,38]. In equilibrium, the net heat flux $\mathbf{q}(t)$ fluctuates around zero along the molecular-dynamics trajectory. To measure thermal conductivity at equilibrium, the GK approach links $\mathbf{K}$ to the dissipation rate of heat-flux fluctuations at the atomic scale via the fluctuation-dissipation theorem. The GK formalism for an anisotropic material can be written as [82]

$$\mathbf{K} = \frac{V}{k_B T^2}\int_0^\infty \langle \mathbf{q}(t) \otimes \mathbf{q}(0)\rangle dt, \quad (11)$$

where $\bar{\Psi}(t) = \langle \mathbf{q}(t) \otimes \mathbf{q}(0)\rangle / \langle \mathbf{q}(0) \otimes \mathbf{q}(0)\rangle$ is a second-order tensor generally known as the heat-flux autocorrelation function (HFACF). HFACF elements are one at the origin and subsequently decay to zero with characteristic time scales proportional to the thermal conductivity of the material. Since the length of the MD trajectory is finite, numerical estimation of $\mathbf{K}$ is usually truncated after t_M, the time corresponding to convergence of HFACF to zero, and it is calculated via [85]

$$K_{ij}(t_M) = \frac{\Delta t V}{k_B T^2}\sum_{m=1}^{M}\frac{1}{s-m}\sum_{n=1}^{s-m}\frac{q_i(m+n)q_j(n)}{\langle q_i(0)q_j(0)\rangle}, \quad (12)$$

where Δt is the heat-flux outputting time step, which is different from the molecular-dynamics time step δt; s is the total number of output steps; t_M is given by $M\Delta t$; and $q_j(n)$ is the jth component of the heat flux at the nth output step.

A number of complications arise when calculating the thermal conductivity using Eq. (12). Due to the finite value of s, imposed by limitations on the disk space and computational expense, thermal conductivity might be erroneously shown to be nonsymmetric. However, $\mathbf{K}$ is mathematically shown to be both positive semidefinite and symmetric [86,87]. This is an artifact of the numerical calculation of HFACF, $\epsilon = |\bar{\Psi}_{ij}(t) - \bar{\Psi}_{ji}(t)| > 0|$ for $i \neq$ j. ϵ can be minimized by increasing s, which requires excessive computational expense. Another way to exclude ϵ is to enforce symmetry via $\Psi_{ij} = (\bar{\Psi}_{ij} + \bar{\Psi}_{ji})/2$. In fact, the ergodicity of equilibrium processes requires $\bar{\Psi}_{ij} = \bar{\Psi}_{ji}$ and, therefore, enforcing symmetry is meaningful. Also, as shown in the insets of Figs. 5(a)–5(d), some oscillations of HFACF might still be present at large time scales ($t > 10^5$ fs). To better understand the nature of these oscillations, we note that the GK relation [Eq. (11)] can be expressed in the frequency domain,

$$\mathbf{K}(\omega) = \frac{V}{k_B T^2}\int_0^\infty \langle \mathbf{q}(t) \otimes \mathbf{q}(0)\rangle e^{i\omega t} dt, \quad (13)$$

where the thermal conductivity can be regarded as the limit of $\mathbf{K}(\omega)$ at zero frequency. Figures 5(a)–5(d) present different elements of $\mathbf{K}(\omega)$ for β-C_2S, C_3S, CH, and a CSH molecular structure with Ca:Si = 1.5. It is noted that the high frequencies in the IV and V bands defined in VDOS (Fig. 2) are absent in $\mathbf{K}(\omega)$. This simply means that the hydroxyl groups and water molecules do not contribute to the oscillations of heat conduction. This is due to the dangling nature of hydroxyl groups, which do not contribute to the propagation of phonons, as discussed later in this section. In the case of K_{11} and K_{22} for β-C_2S and C_3S, the contributing frequencies to the oscillation of thermal conductivity extend over the I, II, and III bands and exhibit distinct peaks. By decomposing Eq. (7) into $q_u = (1/V)\sum_{i=1}^{N} \mathbf{v}_i U_i$ and $q_k = (1/V)\sum_{i=1}^{N} \mathbf{r}_i \dot{U}_i$, Landry *et al.* [88] associated the oscillation in $\mathbf{K}(t)$ to optical zero-wave vector phonons. This explanation is consistent with our observation of the absence of such peaks at low frequencies in β-C_2S and C_3S pertaining to the longitudinal and transverse acoustic phonons. The heat conduction across the interlayer spacing of CH and CSH is more sophisticated. The absence of bonded interaction between the layers, also evidenced in elastic properties ($C_{11} > C_{33}$ and $C_{22} > C_{33}$ following Voigt notation), makes the measurement of K_{33} more complicated. In Figs. 5(c) and 5(d), the optical zero-wave vector phonons contributing to the oscillations of $K_{33}(\omega)$ are only present at two sharp peaks in the I and II bands. Unlike β-C_2S and C_3S, significant peaks, however, emerge at low frequencies. This is the evidence of a complex interplay between acoustic and optical phonons which has also been observed in the study of VDOS of amorphous silica [50]. As shown in the enlarged insets of Figs. 5(a)–5(d), $K_{ii}(\omega)$ decays smoothly at small enough frequencies to its limit value. To estimate this limit thermal conductivity (k_{ij}), we fitted a power function of the form $K_{ij}(\omega) = K_{ij} + \xi\omega^{\zeta}$, where K_{ij}, ξ, and ζ are estimated using the least-squares approach. In addition, ten independent simulations with different initial conditions are performed for each molecular model, and the mean and standard deviation of the thermal-conductivity tensor are computed subsequently. Each simulation is 10 ns long, and $\mathbf{q}(t)$ is recorded every 0.1 fs for CH and CSH, and every 1.0 fs for β-C_2S and C_3S. The thermal conductivity calculated using this method is found to be close to the average value of thermal conductivity in the time domain. A particularity of CSH is that the value of thermal conductivity depends on Δt, the resolution in which $q(t)$ is recorded. In fact, the HFACF plunges very quickly to zero, meaning that the assessment of short time-scale behaviors of $\Psi(t)$ is crucial. To this end,

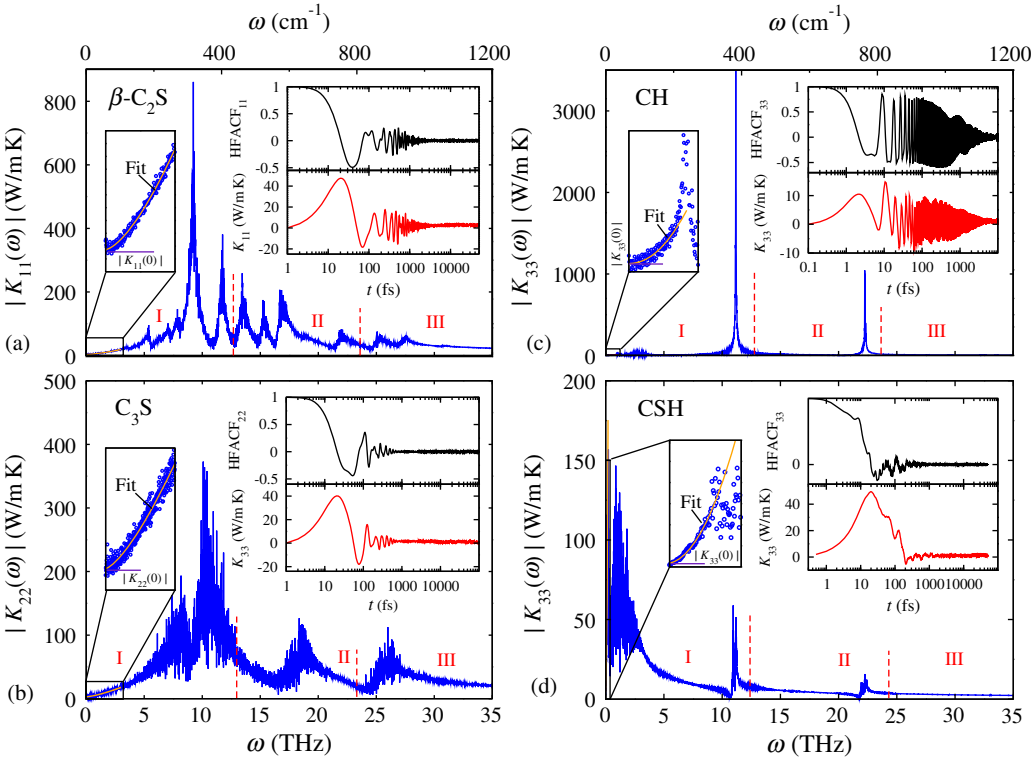

FIG. 5. The power spectra of different components of the thermal conductivity tensor in frequency domain (Fourier transform of the heat-flux autocorrelation function) for β-C_2S, C_3S, CH, and a CSH sample with Ca:Si = 1.5. The insets in black and red correspond to the heat-flux autocorrelation function and the thermal conductivity in time domain, respectively, exhibiting pronounced oscillations in long time-scales. The enlarged inset shows the fitting procedure adopted here to estimate the thermal conductivity at the zero frequency which corresponds to Green-Kubo relation.

we measured the thermal conductivity of CSH with different Δt resolutions using the above method. The true thermal conductivity of CSH is then the limit of $K_{ij}(\Delta t)$ for vanishing Δt values. Specifically, we find that the thermal conductivity of CSH scales linearly with Δt, $K_{ij}(\Delta t) = \zeta \Delta t + K^0_{ij}$, so that the intercept at the origin can be considered to be the actual thermal conductivity of CSH; $K_{ij} = \lim_{\Delta t \to 0} K_{ij}(\Delta t)$.

Following the above procedure, the full thermal-conductivity tensor is computed for all models. In the case of β-C_2S and C_3S, we find $\mathbf{K}$ to be diagonal ($K_{ij} = 0, i \neq j$). Therefore, the [100], [010], and [001] are the same as the principal thermal-conductivity directions. For the CH and CSH models, we generally find that $K_{11} > K_{22} > K_{12}$ and $K_{12} \gg K^0_{13}, K^0_{23}$. Therefore, the thermal conductivity of CH and CSH in a Cartesian coordinate system, where 1, 2, and 3 directions are, respectively, [100], [010], and [001] crystallographic directions, can be approximated as

$$\mathbf{K} \simeq \begin{bmatrix} k_{11} & k_{12} & 0 \\ k_{12} & k_{22} & 0 \\ 0 & 0 & k_{33} \end{bmatrix}. \quad (14)$$

This form of the thermal-conductivity tensor presented in Eq. (14) is not only symmetric but also positive-definite because of the magnitude of the K_{ij} elements. The tensor of thermal conductivity can be expressed in terms of its principal thermal conductivities, the eigenvalues of the $\mathbf{K}$ tensor. The principal thermal-conductivity values for β-C_2S, C_3S, CH, 11-Å tobermorite, and a CSH model are summarized in Table II. The three principal conductivity values for CSH models, $K_{III} < K_{II} < K_I$, are presented in Figs. 5(a)–5(c). While the eigenvectors corresponding to K_I and K_{II} are located in the 12 plane (calcium-silicate layers), the third axis (across the interlayer spacing) is fully aligned with the eigenvector associated with K_{III}. Akin to the anisotropic nature of mechanical properties of CSH [18], the heat-transport properties also show strong anisotropy such that the thermal conductivity in the defective calcium-silicate sheets (12 plane) is statistically larger than that of the out-of-plane direction (third axis). While the xy plane is populated with fairly heat conductive Si—O bonds, looser Ca—O bonds and water molecules in the interlayer space scatter phonons and diminish the heat transport along the z direction, perpendicular to the layers.

Despite the clear presence of anisotropy in heat-transport properties, we find no correlation between the chemical composition and thermal conductivity of CSH in Fig. 6. To this end, we investigate the absence of such correlation via a comparative analysis with crystalline phases. The volume

TABLE II. Transport properties of β-C_2S (belite), C_3S (alite), CH (portlandite), $C_{1.0}SH_{0.5}$ (11-Å tobermorite), and $C_{1.75}SH_{2.0}$ including principal thermal conductivity values, volumetric thermal conductivity, longitudinal, transverse, and volumetric acoustic velocities, and the mean free path of phonons calculated using CSH FF potential.

	K_I (W/m K)	K_{II} (W/m K)	K_{III} (W/m K)	K_v (W/m K)	S_l (km/s)	S_t (km/s)	S_v (km/s)	l_m (Å)
β-C_2S	3.45 ± 0.4	3.45 ± 0.4	3.45 ± 0.4	3.45 ± 0.4	21.4	12.0	13.3	3.2
C_3S	3.35 ± 0.3	3.35 ± 0.3	3.35 ± 0.3	3.35 ± 0.3	22.4	12.6	14.0	2.9
CH	2.00 ± 0.2	1.20 ± 0.2	0.75 ± 0.2	1.32 ± 0.2	14.1	7.0	7.9	1.7
$C_{1.0}SH_{0.5}$	1.25 ± 0.2	0.95 ± 0.2	0.74 ± 0.2	0.98 ± 0.2	19.9	10.2	11.4	1.4
$C_{1.75}SH_{2.0}$	1.25 ± 0.2	0.95 ± 0.2	0.74 ± 0.2	0.98 ± 0.2	19.2	11.67	12.9	1.6

thermal conductivity of CSH does not alter with the Ca:Si ratio and it is close to that of 11-Å tobermorite (see Table II). The above K_v values for CSH are close to those of amorphous silica measured experimentally [89–93] and calculated numerically [94] and theoretically [95,96]. Since the variation of the Ca:Si ratio is merely achieved by removing SiO_2 groups from 11-Å tobermorite, it can be viewed as a parameter that is inversely proportional to the defect content. In the absence of an interface and boundaries in the bulk material, there are two phonon scattering mechanisms: phonon-phonon and phonon-defect scattering. Assuming that different scattering processes are independent, Matthiessen's rule combines the two scattering mechanisms to an effective process using

$$\frac{1}{l_m} = \frac{1}{\bar{l}_{\text{ph-vacancy}}} + \frac{1}{\bar{l}_{\text{ph-ph}}}, \tag{15}$$

where l_m is the mean free path of phonons and $\bar{l}_{\text{ph-vacancy}}$ is the mean phonon-vacancy scattering length, the distance that a phonon travels prior to being scattered off a vacancy defect. $\bar{l}_{\text{ph-ph}}$ is the mean phonon-phonon scattering length, the distance that a phonon travels before being scattered by another phonon. Matthiessen's rule specifies two limiting regimes for phonon transport in a material: vibration-dominated ($\bar{l}_{\text{ph-ph}} \ll \bar{l}_{\text{ph-vacancy}}$) and defect-dominated ($\bar{l}_{\text{ph-vacancy}} \ll \bar{l}_{\text{ph-ph}}$) regimes. Therefore, if a material is in the vibration-dominated regime, then the population of defects would not affect the heat-transport properties. Here, the kinetic theory formulation of heat transport can be used to estimate the characteristic length scale of phonons [97],

$$K_v = \tfrac{1}{3}\rho C_v S_v l_m, \tag{16}$$

where S_v is the speed of sound estimated by averaging the longitudinal and transverse sound velocities, S_l and S_t, respectively, using [98]

$$S_v = \left[\frac{1}{3}\left(\frac{1}{S_l^3} + \frac{2}{S_t^3}\right)\right]^{-1/3}, \tag{17}$$

where $S_l = \sqrt{(4g + 3k)/3\rho}$ and $S_t = \sqrt{g/\rho}$ are the polycrystalline averages of these acoustic velocities computed from the bulk k and shear g moduli and the density presented in Table I and the Supplemental Material [40], Table VI. The acoustic velocities and mean free path of phonons for β-C_2S, C_3S, CH, 11-Å tobermorite, and a CSH model are provided in Table II. The mean free path of CSHs and CH is almost half of that of β-C_2S and C_3S. The space-filling structure of the clinker phases explains their relatively high thermal conductivity and the mean free path of

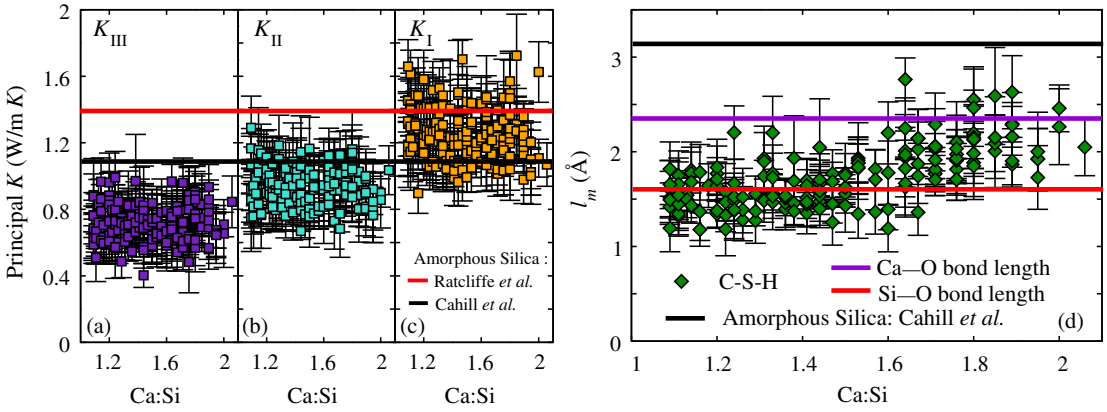

FIG. 6. The anisotropic nature of thermal conduction in CSH and the effect of stoichiometry on the principal thermal conductivity values (a) K_I, (b) K_{II}, and (c) K_{III} compared against the experimental values of thermal conductivity of amorphous silica measured by Cahill *et al.* [89] and Ratcliffe [90]. (d) The mean free path of phonons (l_m) in CSH compared against mean free path of phonons in amorphous silica as measured by Cahill *et al.* [89,91], Ca—O and Si—O bond lengths.

the phonons. The thermal conductivity values observed for β-C_2S and C_3S are close to the thermal conductivity of crystalline silica [90]. However, the layered structure of CSH and CH scatters phonons across the interlayer spacing and significantly reduces the heat transport properties. In fact, l_m is on the order of Si—O and Ca—O bond lengths ($d_{\mathrm{Si—O}} = 1.62$ Å and $d_{\mathrm{Ca—O}} = 2.42$ Å) across the range of considered Ca:Si ratios in CSH, which agrees with experimental measurements of Cahill *et al.* [89,96] for fused silica. Therefore, it can be safely assumed that heat transport in CSH and CH is in the vibration-dominated regime [Fig. 6(d)]. This explains why the Ca:Si ratio (or, in other words, the defect content) does not significantly alter the thermal conductivity of CSH. Moreover, the absence of a phonon-defect-scattering mechanism satisfies the scale separability condition and justifies the use of mean-field homogenization theories for upscaling purposes.

VI. MACROSCALE THERMAL PROPERTIES

In Secs. IV and V, we explored the effect of chemistry on the nanoscale equilibrium and nonequilibrium thermophysical properties of various calcium-silicate phases present in cement paste. In this section, we employ multiscale modeling techniques to link the nanoscale properties of individual constituent phases of cement paste to macroscale properties [79,99–103]. The upscaling of specific-heat capacity from the atomic scale (level 0) to the macroscale (level 3) is rather straightforward. Since energy and volume are extensive thermodynamic quantities, they can be written as the sum of those quantities for individual phases in a composite material. Therefore, the constant-pressure specific-heat capacity of a composite can be considered as a linear combination of that of individual phases. This also holds true during the course of chemical reaction involving m reactive agents (R_i) and n reaction products (P_i),

$$\alpha_1 R_1 + \cdots + \alpha_m R_m \rightarrow \beta_1 P_1 + \cdots + \beta_n P_n, \tag{18}$$

where α_i and β_i are the number of moles of reactants and products in the balanced stoichiometry, respectively. Investigations on the properties of a mixture of reactants and products can be performed in terms of reaction degree η, i.e., the mass of reactants at a given time divided by the total mass of reactants and products. Hence, the constant-pressure specific-heat capacity of a mixture of reactants and products in terms of reaction degree can be written as

$$c_p^{\mathrm{mix}} = (1-\eta)\sum_{i=1}^{m} \phi_{R_i} c_p^{R_i} + \eta \sum_{i=1}^{m} \phi_{P_i} c_p^{P_i}, \tag{19}$$

where $c_p^{R_i}$ and $c_p^{P_i}$ are constant-pressure specific-heat capacities of, respectively, the ith reactant and product. $\phi_{R_i} = \alpha_i M_{R_i}/\sum_i \alpha_i M_{R_i}$ and $\phi_{P_i} = \beta_i M_{P_i}/\sum_i \beta_i M_{P_i}$ are the mass fractions of the ith reactant and product with molar mass M_{R_i} and M_{P_i}, respectively. Traditionally, cement paste is regarded as a composite of anhydrous clinker phases and hydration products that, in the case of CSH, is a nonstoichiometric product [25]. To simplify the complex cement hydration reaction, we assume a constant stoichiometry for the resultant CSH. Therefore, the hydration process is written as [25]

$$C_2S + zH \rightarrow C_{1.7}SH_{1.9} + 0.3CH + (z-2.2)H, \tag{20}$$

$$C_3S + zH \rightarrow C_{1.7}SH_{1.9} + 1.3CH + (z-3.2)H, \tag{21}$$

where z is the number of water moles used in the hydration and $C_{1.7}SH_{1.9}$ is the common form of CSH in OPC systems. In the current work, we neglect the impact on thermal properties of cement paste from aluminate phases such as C_3A and C_4AF and their hydration products.

By juxtaposing Eqs. (18)–(21) and using the specific-heat-capacity values provided in Table I, the constant-pressure specific-heat capacity of hydrating cement paste can be estimated in terms of hydration degree. Figure 7 presents the constant-pressure specific-heat capacities of three hydrating cement pastes with water-to-cement ratios (w/c) of 0.3, 0.4, and 0.5 and their comparison with macroscopic experimental measurements of Bentz [7]. According to Eq. (19), simulation results are necessarily linear in terms of η and are in qualitatively good agreement with the experimental measurements. The slight difference between the experiment and simulation are attributed to the presence of other phases in OPC systems and the difference between the properties of bulk and interfacial water. Nevertheless, both simulation and experiments indicate that the heat capacity of the paste decreases with increasing hydration degree. This can be understood by proper consideration of the role of water during the course of hydration. The specific-heat capacity of bulk water is considerably high (4.18 J/g K), which makes the heat

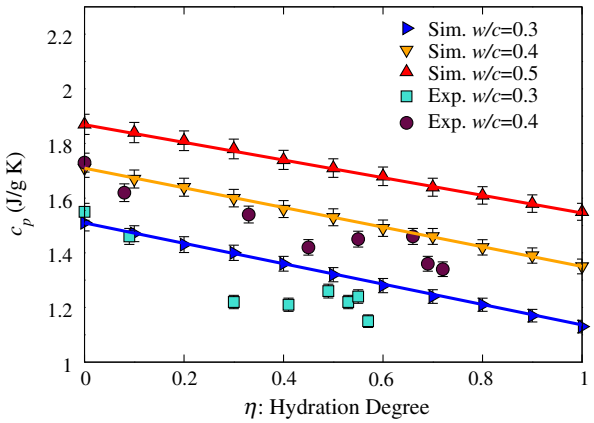

FIG. 7. The effect of hydration degree on the macroscopic specific-heat capacity of hydrating cement paste for three water-to-cement ratios (w/c). The simulation results derived from atomistic simulation and mixture laws are compared with experimental measurements of Bentz [7] for $w/c = 0.3$ and 0.4.

capacity of the mixture of water and clinker relatively high. Throughout the hydration process, the water is consumed to precipitate CSH, which has significantly lower specific-heat capacity (see Fig. 4). Also, part of this water is trapped within the CSH molecular structure, which exhibits features of supercooled water with considerably lower specific-heat capacity compared to that of room-temperature bulk water (see the inset of Fig. 4). Following the same lines of thought, we infer that the heat capacity of cement paste increases with increasing w/c ratio. This is confirmed by both simulation and experiment and can be rationalized in the sense that the portion of water that does not contribute to hydration is trapped in the interparticle and capillary pores. The large specific-heat capacity of unreacted water in such pores increases the heat capacity of the cement paste.

Since heat flux is an intensive thermodynamic quantity, simple composition-based mixture rules are not suitable for upscaling heat-transport properties in composite materials. Fortunately, mean-field homogenization theories present a consistent mechanophysical framework to upscale such properties in multiphase and multiscale materials. These micromechanical models [105] are based on the pioneering work of Eshelby [104], which considers an ellipsoidal inclusion embedded in an infinite isotropic matrix. From the homogenized conductivity viewpoint, the system of randomly oriented anisotropic ellipsoidal inclusions embedded in an isotropic matrix with perfect interfaces between matrix and inclusions K_v^M is indistinguishable from the system of spherical inclusions with a volume thermal conductivity K_v (see the Supplemental Material [40] for the derivations of micromechanics models). Therefore, after proper orientational averaging, the homogenized thermal conductivity of matrix-inclusion morphology (known as the Mori-Tanaka scheme) K_v^{MT} reduces to

$$K_v^{\mathrm{MT}} = \frac{f_M K_v^M + \sum_{s=1}^{n_p} f_s K_v^s A_s^{\mathrm{sph}}}{f_v^M + \sum_{s=1}^{n_p} f_s A_s^{\mathrm{sph}}}, \tag{22}$$

where n_p, f_s, and $A_s^{\mathrm{sph}} = 3K_v^M/(2K_v^M + K_v^s)$ are, respectively, the number of inclusion phases, the volume fraction, and the spherical localization factor of the sth phase. Similarly, the homogenized thermal conductivity for self-consistent morphology K_v^{SC} reduces to

$$K_v^{\mathrm{SC}} = \frac{\sum_{s=1}^{n_p} f_s K_v^s B_s^{\mathrm{sph}}}{\sum_{s=1}^{n_p} f_s B_s^{\mathrm{sph}}}, \tag{23}$$

where $B_s^{\mathrm{sph}} = 3K_v^{\mathrm{SC}}/(2K_v^{\mathrm{SC}} + K_v^s)$ is the spherical localization factor of the sth phase. It is instructive to note that the mathematical formula for K_v^{SC} has an implicit nature requiring an iterative procedure to obtain the solutions.

As discussed in Sec. I and schematically shown in Fig. 1(b), the CSH paste at the mesoscale is assumed to be comprised of randomly oriented polydisperse CSH particles with an average size of roughly 5 nm. The characteristic length of these nanoparticles is much smaller than the size of the microscale representative elementary volume and much larger than the mean free path of phonons in the order of Si—O and Ca—O bonds. This means that the conditions of scale separability are fully met between the nano-, meso-, and microscales. Therefore, the microthermoporomechanics formulation introduced above is suitable for homogenization of thermal conductivity of CSH at the mesoscale. Based on the results presented in Fig. 6, the principal thermal-conductivity values of CSH are normally distributed and uncorrelated. Hence, we can treat Eq. (23) in a probabilistic fashion by randomly choosing the principal thermal-conductivity values of the CSH particles from normal distributions. Here, we utilize a Monte-Carlo-uncertainty-propagation scheme to measure both the expectations and standard deviations of the homogenized thermal-conductivity values at microscale. Figure 8(a) presents the homogenized thermal conductivity of CSH paste at microscale for two limiting cases of fully saturated and dry mesopores, as a function of the CSH packing density, $\zeta = 1 - \varphi$, where φ is the mesoporosity. Since the bulk thermal conductivity values of air and water are lower than that of CSH, the thermal conductivity of CSH paste decreases with increasing porosity. Note that in nanoporous media in contact with the outside air, the composition of confined air will not be that of the outside air. When engineering the CSH heat conduction properties, there are two design parameters: the mesostructure design and the saturation degree of mesopores. Constantinides and Ulm [16] showed that CSH nanoparticles coalesce at 64% and 76% packing fractions, attributing them to low-density (LD) and high-density (HD) CSHs. Given the two limiting saturation levels and the two packing fractions, the upper and lower bounds of CSH paste's thermal conductivity can be identified. These bounds are displayed by numbered red and black rectangles in Fig. 8(a), where the saturated HD (rectangle 1) and dry LD (rectangle 4) CSHs have, respectively, the highest and lowest homogenized thermal conductivity values.

The cement paste at microscale can be assumed to be a multiphase composite consisting of CSH paste embracing anhydrous clinker phases, portlandite, and fluid inside capillary pores [see Fig. 1(c) and relevant discussion in Sec. I]. The microstructure of cement paste at this scale is akin to that of a matrix-inclusion morphology. Therefore, the Mori-Tanaka scheme would be the method of choice for upscaling the thermal conductivity of individual phases at microscale (level 2) to that of macroscale (level 3). Over the course of cement hydration [see Eqs. (20), (21), (18)], the volume fractions of individual phases (f_i) (reactant or product) are known from the reaction degree η and their mass density ρ_i (see Table I). Therefore, the homogenized thermal conductivity of cement paste can be implicitly expressed in terms of hydration degree and

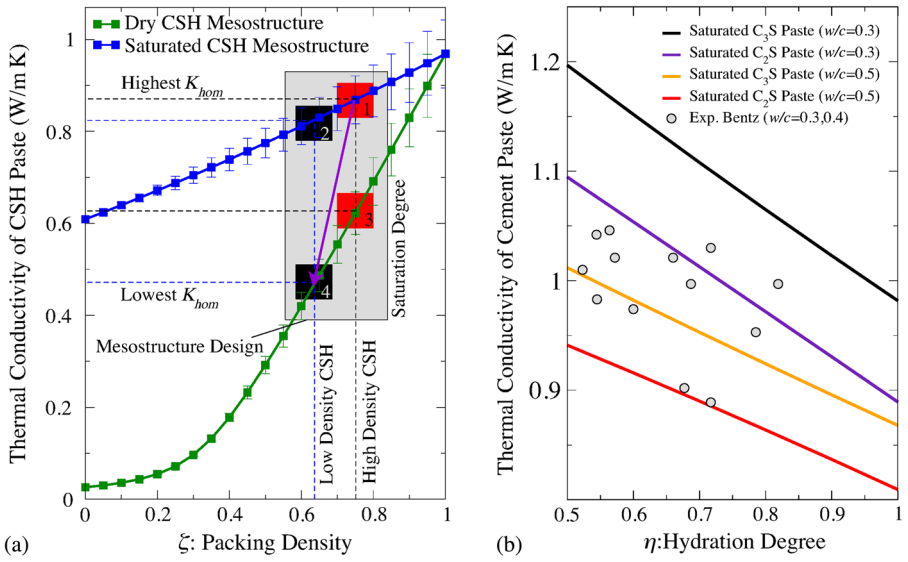

FIG. 8. The mean-field homogenization of thermal conductivity values at the meso- and microscales. (a) The effects of CSH mesostructure (packing density) and saturation degree on the thermal conductivity of CSH paste estimated via probabilistic microthermoporomechanics. (b) The effect of w/c ratio, saturation degree, and the type of clinker phase on macroscale thermal conductivity of hydrating cement paste compared with experimental measurements of Bentz [7] for hydrating cement pastes.

the thermal-conductivity values of individual phases (Table II) through Eq. (22). Figure 8(b) presents the thermal conductivity as a function of hydration degree for resulting cement pastes produced from the hydration of pure C_2S and C_3S clinkers at different w/c ratios ($w/c = 0.3$ and 0.5) for saturated meso- and micropores compared with experimental measurements of Bentz [7] for cement of varying w/c ratio and curing conditions. Here, we focus on later stages of hydration ($0.5 < \eta < 1$) as other modes of heat transport related to dissolution and precipitation mechanisms are rather negligible. We observe that the thermal conductivity of cement paste decreases with increasing hydration degree in agreement with experimental observations of Mounanga *et al.* as a function of hydration time [106]. This is because thermal-conductivity values of clinker phases are higher than those of hydration products (CSH and CH). Figure 8(b) indicates that the macroscopic thermal conductivity of cement paste decreases with increasing w/c ratio in full agreement with recent experiments of Maruyama and Igarashi [10]. While the volume fraction of portlandite decreases with increasing w/c ratio, the volume fraction of unreacted water increases. Considering that the thermal conductivity of bulk water is less than that of portlandite, then it would make sense that the thermal conductivity of cement paste at macroscale decreases with increasing w/c ratio.

VII. CONCLUSIONS

In this work, thermal properties of cement paste are studied via a multiscale bottom-up approach, starting from the nanoscale by calculating properties of individual constituent phases and connecting them to macroscale properties using mean-field homogenization theories. At the nanoscale, the phonon density of states of CSHs, CH, β-C_2S, and C_3S and the components' atomic contributions are studied in detail via the diagonalization of the dynamical matrix and velocity autocorrelation functions. Analogous to glassy materials, we find CSH to exhibit excess of vibrational states characterized by the boson peak at the low-frequency region. The position of the boson peak shifts to higher frequencies with increasing CSH density or, equivalently, by decreasing the Ca:Si ratio. The constant volume and pressure specific-heat capacities are calculated for individual phases including 11-Å tobermorite. We find that the specific-heat capacity of dry and saturated CSH models increases linearly with the Ca:Si ratio. The apparent heat capacity of nanoconfined water in the interlayer spacing of CSH is determined to be significantly lower than that of bulk water at room temperature due to strong interaction with the calcium-silicate substrate. We measure the full thermal-conductivity tensor of individual phases using the Green-Kubo relation. The Fourier transformation of the heat-flux autocorrelation function reveals long-lasting sharp frequencies associated with optical phonons with zero group velocities that do not contribute to the thermal conduction in these complex systems. In addition, the mean free path of phonons in different phases are estimated to be on the order of Si—O and Ca—O bond lengths. The short mean free path of phonons in the cement-paste-constituent phases meets the condition of scale separability. We demonstrate the variation of the macroscopic heat capacity of cement paste in terms of the hydration degree using mixture rules. The macroscopic heat-capacity values predicted via our multiscale bottom-up

approach are in good qualitative agreement with experiments. We show that the homogenized thermal conductivity of CSH paste at microscale is only affected by the packing density and the saturation level of the CSH mesopores. Our theoretical study indicates that the macroscopic thermal-conductivity values should decrease with increasing w/c ratio in later stages of hydration degree. Overall, this work provides a bottom-up framework for upscaling thermal properties with potentially broad applications in multiscale and multiphase porous materials.

ACKNOWLEDGMENTS

The Concrete Sustainability Hub at MIT has supported this work with sponsorship provided by the Portland Cement Association (PCA) and the National Ready Mixed Concrete Association (NRMCA) Research and Education Foundation. This work has been partly carried out within the framework of the ICoME2 Labex (ANR-11-LABX-0053) and the A*MIDEX projects (ANR-11-IDEX-0001-02), cofunded by the French program "Investissements d'Avenir," which is managed by the ANR, the French National Research Agency. With great pleasure, we acknowledge discussions with Dr. Davoud Ebrahimi, Dr. Konrad Krakowiak, Dr. Andrej Kosmirlj, Dr. Andres Saul, Dr. Benoit Coasne, Dr. Jeff Thomas, Dr. Mathieu Bauchy, and Prof. Hamlin Jennings, Prof. Henri Vandamme, and Prof. Sidney Yip.

[1] F. Ulm and O. Coussy, What is a "massive" concrete structure at early ages? Some dimensional arguments, J. Eng. Mech. **127**, 512 (2001).

[2] Mohammad Javad Abdolhosseine Qomi, Arash Noshadravan, Jake Sobstyl, Jameson Toole, J. Ferreira, R. J.-M. Pellenq, F.-J. Ulm, and Marta C. Gonzalez, "Data Analytics for Energy Efficient Retrofits of Cities" (unpublished).

[3] G. De Schutter and L. Taerwe, Specific heat and thermal diffusivity of hardening concrete, Mag. Concr. Res. **47**, 203 (1995).

[4] Kook-Han Kim, Sang-Eun Jeon, Jin-Keun Kim, and Sungchul Yang, An experimental study on thermal conductivity of concrete, Cem. Concr. Res. **33**, 363 (2003).

[5] Ramazan Demirboga and Rustem Gul, The effects of expanded perlite aggregate, silica fume and fly ash on the thermal conductivity of lightweight concrete, Cem. Concr. Res. **33**, 723 (2003).

[6] Ramazan Demirboğa, Influence of mineral admixtures on thermal conductivity and compressive strength of mortar, Energy Build. **35**, 189 (2003).

[7] D. P. Bentz, Transient plane source measurements of the thermal properties of hydrating cement pastes, Mater. Construc. Mater. Structures **40**, 1073 (2007).

[8] Seyoon Yoon, Donald E. Macphee, and Mohammed S. Imbabi, Estimation of the thermal properties of hardened cement paste on the basis of guarded heat flow meter measurements, Thermochim. Acta **588**, 1 (2014).

[9] D. Mikulic, B. Milovanovic, and I. Gabrijel, in *Nondestructive Testing of Materials and Structures*, RILEM Bookseries Vol. 6, edited by Oguz Gunes and Yılmaz Akkaya (Springer Netherlands, Dordrecht, 2013) pp. 465–471.

[10] Ippei Maruyama and Go Igarashi, Cement reaction and resultant physical properties of cement paste, J. Adv. Concr. Technol. **12**, 200 (2014).

[11] Yunsheng Xu and D. D. L. Chung, Effect of sand addition on the specific heat and thermal conductivity of cement, Cem. Concr. Res. **30**, 59 (2000).

[12] A. Abdelalim, S. Abdallah, K. Easawi, S. Negm, and H. Talaat, Thermal properties of hydrated cement pastes studied by the photoacoustic technique, J. Phys. Conf. Ser. **214**, 012136 (2010).

[13] E. Masoero, E. Del Gado, R. J.-M. Pellenq, F.-J. Ulm, and S. Yip, Nanostructure and Nanomechanics of Cement: Polydisperse Colloidal Packing, Phys. Rev. Lett. **109**, 155503 (2012).

[14] Andrew J. Allen, Jeffrey J. Thomas, and Hamlin M. Jennings, Composition and density of nanoscale calcium-silicate-hydrate in cement, Nat. Mater. **6**, 311 (2007).

[15] W.-S. Chiang, G. Ferraro, E. Fratini, F. Ridi, Y.-Q. Yeh, U-S. Jeng, S.-H. Chen, and P. Baglioni, Multiscale structure of calcium- and magnesium-silicate-hydrate gels, J. Mater. Chem. A **2**, 12991 (2014).

[16] Georgios Constantinides and Franz-Josef Ulm, The nanogranular nature of C-S-H, J. Mech. Phys. Solids **55**, 64 (2007).

[17] Luc Dormieux, Djimedo Kondo, and Franz-Jozef Ulm, *Microporomechanics*, 1st ed. (Wiley, Hoboken, NJ, 2006).

[18] M. J. Abdolhosseini Qomi, K. J. Krakowiak, M. Bauchy, K. L. Stewart, R. Shahsavari, D. Jagannathan, D. B. Brommer, A. Baronnet, M. J. Buehler, S. Yip, F.-J. Ulm, K. J. Van Vliet, and R. J.-M. Pellenq, Combinatorial molecular optimization of cement hydrates, Nat. Commun. **5**, 4960 (2014).

[19] M. Bauchy, M. J. Abdolhosseini Qomi, F.-J. Ulm, and R. J.-M. Pellenq, Order and disorder in calcium-silicate-hydrate, J. Chem. Phys. **140**, 214503 (2014).

[20] Mathieu Bauchy, Mohammad Javad Abdolhosseini Qomi, Christophe Bichara, Franz-Joseph Ulm, and Roland J.-M. Pellenq, Nanoscale structure of cement: Viewpoint of rigidity theory, J. Phys. Chem. C **118**, 12485 (2014).

[21] M. Bauchy, M. J. Abdolhosseini Qomi, C. Bichara, F.-J. Ulm, and R. J.-M. Pellenq, arXiv:1410.2916.

[22] M. Bauchy, H. Laubie, M. J. Abdolhosseini Qomi, C. G. Hoover, F.-J. Ulm, and R. J.-M. Pellenq, Fracture toughness of calcium-silicate-hydrate from molecular dynamics simulations, J. Non-Cryst. Solids **419**, 58 (2015).

[23] Mathieu Bauchy, Mohammad Javad Abdolhosseine Qomi, Christophe Bichara, F. J. Ulm, and Roland J.-M. Pellenq, Rigidity Transition in Materials: Hardness Is Driven by Weak Atomic Constraints, Phys. Rev. Lett. **114**, 125502 (2015).

[24] Mohammad Javad Abdolhosseini Qomi, Mathieu Bauchy, Franz-Josef Ulm, and Roland J.-M. Pellenq, Anomalous composition-dependent dynamics of nanoconfined water

in the interlayer of disordered calcium-silicates, J. Chem. Phys. **140**, 054515 (2014).
[25] H. F. W. Taylor, *Cement Chemistry*, 2nd ed. (Thomas Telford, London, 1997).
[26] M. Bigaré, A. Guinier, C. Maziéres, M. Regourd, N. Yannaquis, W. Eysbl, Th. Hahn, and E. Woermann, Polymorphism of tricalcium silicate and its solid solutions, J. Am. Ceram. Soc. **50**, 609 (1967).
[27] Ángeles G. De La Torre, Sebastián Bruque, Javier Campo, and Miguel A. G. Aranda, The superstructure of C_3S from synchrotron and neutron powder diffraction and its role in quantitative phase analyses, Cem. Concr. Res. **32**, 1347 (2002).
[28] D. K. Smith, A. Majumdar, and F. Ordway, The crystal structure of dicalcium silicate, Acta Crystallogr. **18**, 787 (1965).
[29] C. M. Midgley, The crystal structure of dicalcium silicate, Acta Crystallogr. **5**, 307 (1952).
[30] K. E. Hudson and G. W. Groves, The structure of alite in portland cement clinker—TEM evidence, Cem. Concr. Res. **12**, 61 (1982).
[31] Hegoi Manzano, Engin Durgun, Mohammed Javad Abdolhosseine Qomi, Franz-Josef Ulm, Roland. J. M. Pellenq, and Jeffrey. C. Grossman, Impact of chemical impurities on the crystalline cement clinker phases determined by atomistic simulations, Cryst. Growth Des. **11**, 2964 (2011).
[32] D. M. Henderson and S. H. Gutowsky, A nuclear magnetic resonance determination of the hydrogen positions in $Ca(OH)_2$, Am. Mineral. **47**, 1231 (1962).
[33] Sa Hamid, The crystal-structure of the 11a natural tobermorite $Ca_{2.25}[Si_3O_{7.5}(OH)_{1.5}]H_2O$, Z. Kristallogr. **154**, 189 (1981).
[34] Mohammad Javad Abdolhosseini Qomi, Franz-Josef Ulm, and Roland J.-M. Pellenq, Evidence on the dual nature of aluminum in the calcium-silicate-hydrates based on atomistic simulations, J. Am. Ceram. Soc. **95**, 1128 (2012).
[35] György Hantal, Laurent Brochard, Hadrien Laubie, Davoud Ebrahimi, Roland J.-M. Pellenq, Franz-Josef Ulm, and Benoit Coasne, Atomic-scale modelling of elastic and failure properties of clays, Mol. Phys. **112**, 1294 (2014).
[36] S. Plimpton, Fast parallel algorithms for short-range molecular dynamics, J. Comput. Phys. **117**, 1 (1995).
[37] J. D. Gale, GULP: A computer program for the symmetry-adapted simulation of solids, J. Chem. Soc., Faraday Trans. 2 **93**, 629 (1997).
[38] J. D. Gale and A. L. Rohl, The General Utility Lattice Program (GULP), Mol. Simul. **29**, 291 (2003).
[39] Rouzbeh Shahsavari, Roland J.-M. Pellenq, and Franz-Josef Ulm, Empirical force fields for complex hydrated calcio-silicate layered materials, Phys. Chem. Chem. Phys. **13**, 1002 (2011).
[40] See Supplemental Material at http://link.aps.org/supplemental/10.1103/PhysRevApplied.3.064010 for details of the force field, its transferability to crystalline phases, and the microthermoporomechanics model.
[41] D. Wolf, P. Keblinski, S. R. Phillpot, and J. Eggebrecht, Exact method for the simulation of Coulombic systems by spherically truncated, pairwise r1 summation, J. Chem. Phys. **110**, 8254 (1999).
[42] G. Constantinides and F. J. Ulm, The effect of two types of C-S-H on the elasticity of cement-based materials: Results from nanoindentation and micromechanical modeling, Cem. Concr. Res. **34**, 67 (2004).
[43] Paul Acker, in *Creep, Shrinkage, and Durability Mechanics of Concrete and Other Quasi-Brittle Materials* (Elsevier, London, 2001), pp. 15–25.
[44] F. H. Wittmann, Estimation of the modulus of elasticity of calcium hydroxide, Cem. Concr. Res. **16**, 971 (1986).
[45] Paulo J. M. Monteiro and C. T. Chang, The elastic moduli of calcium hydroxide, Cem. Concr. Res. **25**, 1605 (1995).
[46] Karine Velez, Sandrine Maximilien, Denis Damidot, Gilbert Fantozzi, and Fransois Sorrentino, Determination by nanoindentation of elastic modulus and hardness of pure constituents of portland cement clinker, Cem. Concr. Res. **31**, 555 (2001).
[47] B. Mihailova, N. Zotov, M. Marinov, J. Nikolov, and L. Konstantinov, Vibrational spectra of rings in silicate glasses, J. Non-Cryst. Solids **168**, 265 (1994).
[48] Hendrik J. Monkhorst and James D. Pack, Special points for Brillouin-zone integrations, Phys. Rev. B **13**, 5188 (1976).
[49] Ping Yu, R. James Kirkpatrick, Brent Poe, Paul F. McMillan, and Xiandong Cong, Structure of calcium silicate hydrate (C-S-H): Near-, mid-, and far-infrared spectroscopy, J. Am. Ceram. Soc. **82**, 742 (1999).
[50] S. N. Taraskin and S. R. Elliott, Nature of vibrational excitations in vitreous silica, Phys. Rev. B **56**, 8605 (1997).
[51] Francesco Sette, Michael H. Krisch, Claudio Masciovecchio, Giancarlo Ruocco, and Giulio Monaco, Dynamics of glasses and glass-forming liquids studied by inelastic x-ray scattering, Science **280**, 1550 (1998).
[52] R. C. Zeller and R. O. Pohl, Thermal conductivity and specific heat of noncrystalline solids, Phys. Rev. B **4**, 2029 (1971).
[53] A. P. Sokolov, U. Buchenau, W. Steffen, B. Frick, and A. Wischnewski, Comparison of Raman- and neutron-scattering data for glass-forming systems, Phys. Rev. B **52**, R9815 (1995).
[54] Hiroshi Shintani and Hajime Tanaka, Universal link between the boson peak and transverse phonons in glass, Nat. Mater. **7**, 870 (2008).
[55] T. S. Grigera, V. Martín-Mayor, G. Parisi, and P. Verrocchio, Phonon interpretation of the boson peak in supercooled liquids, Nature (London) **422**, 289 (2003).
[56] E. Duval, A. Boukenter, and T. Achibat, Vibrational dynamics and the structure of glasses, J. Phys. Condens. Matter **2**, 10227 (1990).
[57] Hajime Tanaka, Physical origin of the boson peak deduced from a two-order-parameter model of liquid, J. Phys. Soc. Jpn. **70**, 1178 (2001).
[58] U. Buchenau, N. Nücker, and A. J. Dianoux, Neutron Scattering Study of the Low-Frequency Vibrations in Vitreous Silica, Phys. Rev. Lett. **53**, 2316 (1984).
[59] Bertrand Guillot and Yves Guissani, Boson Peak and High Frequency Modes in Amorphous Silica, Phys. Rev. Lett. **78**, 2401 (1997).
[60] D. A. Parshin, H. R. Schober, and V. L. Gurevich, Vibrational instability, two-level systems, and the boson peak in glasses, Phys. Rev. B **76**, 064206 (2007).

[61] N. J. Tao, G. Li, X. Chen, W. M. Du, and H. Z. Cummins, Low-frequency Raman-scattering study of the liquid-glass transition in aqueous lithium chloride solutions, Phys. Rev. A **44**, 6665 (1991).

[62] D. Engberg, A. Wischnewski, U. Buchenau, L. Börjesson, A. J. Dianoux, A. P. Sokolov, and L. M. Torell, Origin of the boson peak in a network glass B_2O_3, Phys. Rev. B **59**, 4053 (1999).

[63] A. Wischnewski, U. Buchenau, A. J. Dianoux, W. A. Kamitakahara, and J. L. Zarestky, Sound-wave scattering in silica, Phys. Rev. B **57**, 2663 (1998).

[64] S. Sugai and A. Onodera, Medium-Range Order in Permanently Densified SiO_2 and GeO_2 Glass, Phys. Rev. Lett. **77**, 4210 (1996).

[65] P. Jund and R. Jullien, Densification effects on the boson peak in vitreous silica: A molecular-dynamics study, J. Chem. Phys. **113**, 2768 (2000).

[66] A. Monaco, A. I. Chumakov, G. Monaco, W. A. Crichton, A. Meyer, L. Comez, D. Fioretto, J. Korecki, and R. Rüffer, Effect of Densification on the Density of Vibrational States of Glasses, Phys. Rev. Lett. **97**, 135501 (2006).

[67] L. Hong, B. Begen, A. Kisliuk, C. Alba-Simionesco, V. N. Novikov, and A. P. Sokolov, Pressure and density dependence of the boson peak in polymers, Phys. Rev. B **78**, 134201 (2008).

[68] Charles Kittel, *Introduction to Solid State Physics*, 8th ed. (Wiley, Hoboken, NJ, 2004).

[69] Thomas Matschei, Barbara Lothenbach, and Fredrik P. Glasser, Thermodynamic properties of portland cement hydrates in the system CaO-Al_2O_3-SiO_2-$CaSO_4$-$CaCO_3$-H_2O, Cem. Concr. Res. **37**, 1379 (2007).

[70] Siavash Ghabezloo, Micromechanics analysis of thermal expansion and thermal pressurization of a hardened cement paste, Cem. Concr. Res. **41**, 520 (2011).

[71] John A. Thomas, Joseph E. Turney, Ryan M. Iutzi, Cristina H. Amon, and Alan J. H. McGaughey, Predicting phonon dispersion relations and lifetimes from the spectral energy density, Phys. Rev. B **81**, 081411 (2010).

[72] I. G. Richardson, The calcium silicate hydrates, Cem. Concr. Res. **38**, 137 (2008).

[73] Jeffrey J. Thomas, Hamlin M. Jennings, and Andrew J. Allen, Relationships between composition and density of tobermorite, jennite, and nanoscale CaO-SiO_2-H_2O, J. Phys. Chem. C **114**, 7594 (2010).

[74] Arnaud C. A. Muller, Karen L. Scrivener, Agata M. Gajewicz, and Peter J. McDonald, Densification of C-S-H measured by ^{1}H NMR relaxometry, J. Phys. Chem. C **117**, 403 (2013).

[75] S. S. Todd, Low-temperature heat capacities and entropies at 298.16 K. of crystalline calcium orthosilicate, zinc orthosilicate and tricalcium silicate, J. Am. Chem. Soc. **73**, 3277 (1951).

[76] Christoph Clauser and Ernst Huenges, in *Rock Physics and Phase Relations*, Vol. 1, edited by Thomas J. Ahrens (American Geophysical Union, New York, 1995), pp. 105–126.

[77] E. Tombari, G. Salvetti, C. Ferrari, and G. P. Johari, Heat capacity of water in nanopores, J. Chem. Phys. **123**, 214706 (2005).

[78] Bruce S. Hemingway, Quartz: Heat capacities from 340 to 1000 K and revised values for the thermodynamic properties, Am. Mineral. **72**, 273 (1987).

[79] M. J. Abdolhosseini Qomi, A. Aghaei, and A. R. Khoei, Multi-scale modeling of surface effect via the boundary Cauchy-Born method, Int. J. Numer. Methods Eng. **85**, 827 (2011).

[80] Takahiro Kuroki, Noboru Kagawa, Harumi Endo, Seizou Tsuruno, and Joseph W. Magee, Specific heat capacity at constant volume for water, methanol, and their mixtures at temperatures from 300 K to 400 K and pressures to 20 MPa, J. Chem. Eng. Data **46**, 1101 (2001).

[81] C. Austen Angell, Insights into phases of liquid water from study of its unusual glass-forming properties, Science **319**, 582 (2008).

[82] Donald A McQuarrie, *Statistical Mechanics*, 1st ed. (Harper and Row, New York, 1975).

[83] Patrick K. Schelling, Simon R. Phillpot, and Pawel Keblinski, Comparison of atomic-level simulation methods for computing thermal conductivity, Phys. Rev. B **65**, 144306 (2002).

[84] Young Hee Lee, R. Biswas, C. M. Soukoulis, C. Z. Wang, C. T. Chan, and K. M. Ho, Molecular-dynamics simulation of thermal conductivity in amorphous silicon, Phys. Rev. B **43**, 6573 (1991).

[85] Konstantin V. Tretiakov and Sandro Scandolo, Thermal conductivity of solid argon from molecular dynamics simulations, J. Chem. Phys. **120**, 3765 (2004).

[86] Joseph M. Powers, On the necessity of positive semidefinite conductivity and Onsager reciprocity in modeling heat conduction in anisotropic media, J. Heat Transfer **126**, 670 (2004).

[87] W. A. Day and Morton E. Gurtin, On the symmetry of the conductivity tensor and other restrictions in the nonlinear theory of heat conduction, Arch. Ration. Mech. Anal. **33**, 26 (1969).

[88] E. S. Landry, M. I. Hussein, and A. J. H. McGaughey, Complex superlattice unit cell designs for reduced thermal conductivity, Phys. Rev. B **77**, 184302 (2008).

[89] D. G. Cahill and R. O. Pohl, Lattice vibrations and heat transport in crystals and glasses, Annu. Rev. Phys. Chem. **39**, 93 (1988).

[90] E. H. Ratcliffe, Thermal conductivities of fused and crystalline quartz, Br. J. Appl. Phys. **10**, 22 (1959).

[91] David G. Cahill, S.-M. Lee, and Torbjorn I. Selinder, Thermal conductivity of κ-Al_2O_3 and α-Al_2O_3 wear-resistant coatings, J. Appl. Phys. **83**, 5783 (1998).

[92] Y. S. Touloukian, *Thermal Conductivity: Nonmetallic Solids*, 1st ed. (Springer, New York, 1971).

[93] A. Eucken, Ann. Phys. (Berlin) **339**, 185 (1911).

[94] Philippe Jund and Rémi Jullien, Molecular-dynamics calculation of the thermal conductivity of vitreous silica, Phys. Rev. B **59**, 13707 (1999).

[95] Philip B. Allen and Joseph L. Feldman, Thermal Conductivity of Glasses: Theory and Application to Amorphous Si, Phys. Rev. Lett. **62**, 645 (1989).

[96] David G. Cahill and R. O. Pohl, Heat flow and lattice vibrations in glasses, Solid State Commun. **70**, 927 (1989).

[97] J. M. Ziman, *Electrons and Phonons: The Theory of Transport Phenomena in Solids*, 1st ed. (Oxford University Press, New York, 2001).

[98] Somnath Bhowmick and Vijay B. Shenoy, Effect of strain on the thermal conductivity of solids, J. Chem. Phys. **125**, 164513 (2006).

[99] A. R. Khoei, M. J. Abdolhosseini Qomi, M. T. Kazemi, and A. Aghaei, An investigation on the validity of Cauchy-Born hypothesis using Sutton-Chen many-body potential, Comput. Mater. Sci. **44**, 999 (2009).

[100] A. Aghaei, M. J. Abdolhosseini Qomi, M. T. Kazemi, and A. R. Khoei, Stability and size-dependency of Cauchy-Born hypothesis in three-dimensional applications, Int. J. Solids Struct. **46**, 1925 (2009).

[101] A. R. Khoei, P. Ghahremani, M. J. Abdolhosseini Qomi, and P. Banihashemi, Stability and size-dependency of temperature-related Cauchy-Born hypothesis, Comput. Mater. Sci. **50**, 1731 (2011).

[102] Davoud Ebrahimi, Andrew J. Whittle, and Roland J.-M. Pellenq, Mesoscale properties of clay aggregates from potential of mean force representation of interactions between nanoplatelets, J. Chem. Phys. **140**, 154309 (2014).

[103] Davoud Ebrahimi, Roland J.-M. Pellenq, and Andrew J. Whittle, Nanoscale elastic properties of montmorillonite upon water adsorption, Langmuir **28**, 16855 (2012).

[104] J. D. Eshelby, The determination of the elastic field of an ellipsoidal inclusion, and related problems, Proc. R. Soc. A **241**, 376 (1957).

[105] H. Hatta and M. Taya, Effective thermal conductivity of a misoriented short fiber composite, J. Appl. Phys. **58**, 2478 (1985).

[106] P. Mounanga, A. Khelidj, and G. Bastian, Experimental study and modelling approaches for the thermal conductivity evolution of hydrating cement paste, Adv. Cem. Res. **16**, 95 (2004).